Modeling of the Vacuum Arc Remelting Process for Estimation and Control of the Liquid Pool Profile

Joseph J. Beaman[1]
Professor
Department of Mechanical Engineering,
University of Texas at Austin,
Austin, TX 78712
e-mail: jbeaman@austin.utexas.edu

Luis Felipe Lopez
Graduate Research Assistant
Department of Mechanical Engineering,
University of Texas at Austin,
Austin, TX 78712
e-mail: felipelopez@utexas.edu

Rodney L. Williamson
Advanced Manufacturing Center,
University of Texas at Austin,
Austin, TX 78712
e-mail: rlwilliamson@mail.utexas.edu

Vacuum arc remelting (VAR) is an industrial metallurgical process widely used throughout the specialty metals industry to cast large alloy ingots. The final ingot grain structure is strongly influenced by the molten metal pool profile, which in turn depends on the temperature distribution in the ingot. A reduced-order model of the solidifying ingot was developed specifically for dynamic control and estimation of the depth of molten liquid pool atop the ingot in a VAR process. This model accounts only for the thermal aspects of the system ignoring other physical domains such as fluid flow and electromagnetic effects. Spectral methods were used to obtain a set of nonlinear dynamic equations which capture the transient characteristics of liquid pool profile variations around a quasi-steady operating condition. These nonlinear equations are then linearized and further simplified by suppressing fast modes. The resulting system was used to construct a linear-quadratic-gaussian (LQG) controller which was tested in a laboratory-scale furnace showing a good performance. A high-fidelity physics-based model is used in real-time to provide information about the solidifying ingot and potential solidification defects.
[DOI: 10.1115/1.4026319]

1 Introduction

1.1 Vacuum Arc Remelting. VAR [1,2] is a secondary melting process used to produce a variety of segregation sensitive and reactive metal alloys (e.g., nickel-base superalloys, titanium, and zirconium alloys). The VAR process is widely used because it is capable of producing fully-dense homogeneous ingots with an appropriate chemistry, physical size, and grain structure. These ingots are free of macrosegregation, porosity, shrinkage cavities, or any other defects associated with uncontrolled solidification during casting. The performance of VAR processed materials depends largely on ingot structure and chemical uniformity [3].

A schematic diagram of the VAR process is shown in Fig. 1. In this process, a cylindrically shaped alloy electrode is loaded into the water-cooled copper crucible of a VAR furnace, the furnace is evacuated, and a DC arc is struck between the electrode (cathode) and some start material (e.g., metal chips) at the bottom of the crucible (anode). The arc heats both the start material and the electrode tip, eventually melting both. As the electrode tip is melted away, molten metal falls through the arc plasma and progressively builds up the ingot in the copper crucible.

During the process, the top of the ingot remains a pool of liquid metal that has a curved cross section. At any moment there exist at least 3 phases: liquid, solid-liquid (mushy zone), and solid. The solidification has to be controlled in order to obtain a sound ingot of good structural quality.

Since the crucible diameter is larger than the electrode diameter, the electrode must be translated downward toward the anode pool to keep the average distance between the electrode tip and pool surface constant. This average distance, called the electrode gap, has an important effect on the heat released during the process because the arc plasma is dependent on the electrode gap. By affecting the distribution of energy and electric current at the surface of the ingot pool, the behavior of the arc influences the ingot solidification conditions, and therefore the quality of the final product.

The impetus for the development of this process has been the need for high-performance, high-purity materials required for aerospace applications. The present day vacuum arc remelting practice for superalloys involves typically, making ingots of 17 in. to 20 in. in diameter. Even larger diameter forging stock is desirable. However, beyond 17 in. ingots of superalloys are increasingly prone to segregation defects known as "freckles" if solidification is not adequately controlled. Kou studied the effect of mushy zone depth and solidification rate on macrosegregation of electroslag remelted ingots [4]. It was reported that macrosegregation increases with increasing depth of mushy zone and decreasing solidification rate (higher local solidification time). A deeper molten metal pool always results in a deeper mushy zone. Shallow pool profiles, on the other hand, result in a different kind of macrosegregation defects called white spots. Hence, it is necessary to understand and control the factors affecting geometry of the molten metal pool and the mushy zone in order to prevent macrosegregation defects from occurring in VAR.

2 Derivation of the Thermal Model

Modeling of VAR has been studied extensively both in the industrial and academic worlds at the macroscale and microscale levels [5–8]. VAR is a multiphysics process that involves not only heat transfer but also fluid dynamics, mass transfer, phase transformations, and electromagnetics [9]. Coupled multiphysics problems tend to be cumbersome because these systems are usually modeled via systems of coupled differential equations which are generally too large for a direct numerical solution; instead the system must be decomposed into a collection of smaller tractable subsystems.

All models in the literature are, in a sense, accurate but they are not suitable for real-time control applications due to the simplifying assumptions used in their development or due to their high computational cost. Recently, a simplified VAR model which

---

[1]Corresponding author.
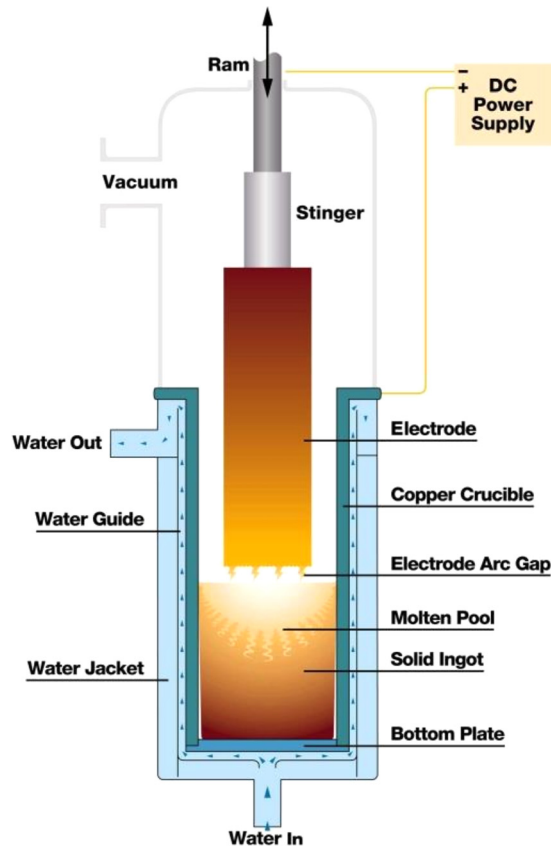
Fig. 1 Schematic diagram of VAR process (courtesy ATI Allvac)

Fig. 2 Schematic of the solidifying ingot

accounts only for heat transfer in the ingot was reported by Kondrashov et al. [10]. The application of this simplified model in the design of an automatic control system for VAR was also suggested but not reported.

A reduced-order model developed specifically for estimation and control purposes is presented in this paper. This model is based on basic axisymmetric remelting (BAR) [6], a compact and accurate explicit finite-volume code used to simulate ingot solidification during a VAR process and known to have a good agreement with experimental results for different ingot sizes and materials [11,12]. BAR is a high-fidelity axisymmetric model that solves conservation equations for charge, mass, momentum, and energy. BAR employs sophisticated electromagnetic and thermal boundary conditions which are intended to capture the effect of the temperature-dependent contact of the VAR ingot with the walls of the crucible.

The approximate thermal model developed in this paper seeks to predict pool profile dynamically when input current and melt efficiency are known. This model has almost the same thermal boundary conditions as in BAR, except for heat fluxes with small overall contributions which have been neglected. The model does not include fluid flow, Joule heating or a temperature-dependent diffusivity in the analysis. Joule heating is known to have a negligible effect in the solidification process, as found with computational simulation. The validity of the simplification of fluid dynamics and electromagnetic processes relies on thermal processes being the slowest, and therefore dictating the dominant dynamics of the overall process. However, by not including convection in the solidifying ingot, an anisotropic phenomenon is being modeled with an isotropic approach.

In this model, only two phases are included: solid and liquid. Melting is assumed to occur at a single average melting temperature (i.e., liquidus temperature is assumed to be equal to solidus temperature), rather than in a broad mushy zone. Densities of
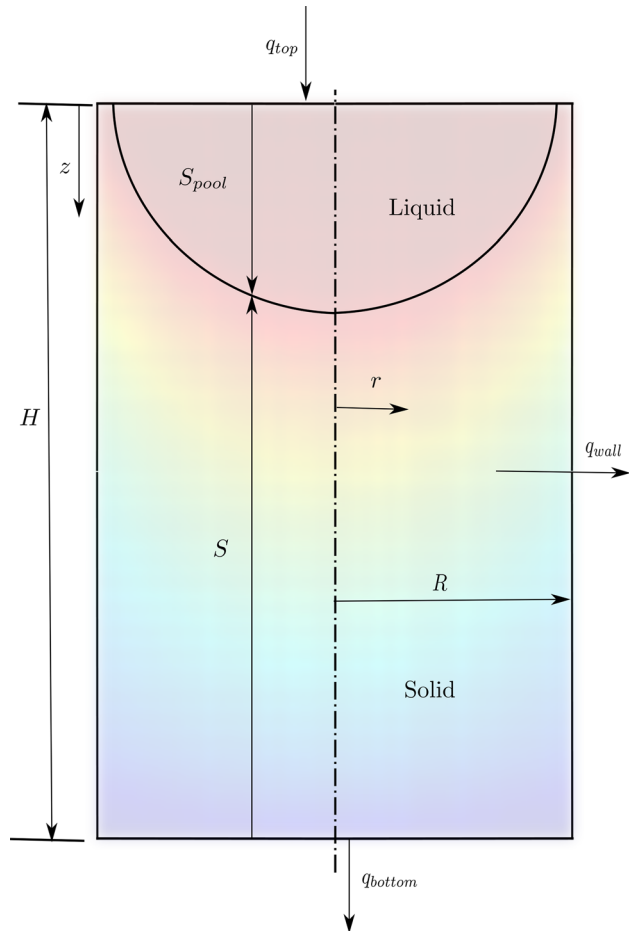
solid and liquid phases are assumed equal. Also, thermal diffusivity is assumed to be constant both for the solid and liquid phases. Thermal diffusivity in the liquid is enhanced to account for convective effects that cannot be modeled through the diffusion equation. In this case, it is assumed that the enhanced liquid thermal diffusivity is 3.0 times greater than that of the alloy at the liquidus temperature.

A schematic of the solidifying ingot is shown in Fig. 2. The solidification dynamics can be modeled using conservation of mass and energy, as described in the following set of equations:

$$\dot{H} = V_i \tag{1}$$

$$V_i = \frac{\dot{m}_e}{\rho A_i} \tag{2}$$

$$\frac{\partial h}{\partial t} = \nabla \cdot (\alpha \nabla h) \tag{3}$$

The system of equations will be solved for the enthalpy distribution in the ingot, $h(z,r,t)$, subject to the boundary conditions

$$-\alpha \frac{\partial h}{\partial z}(H, r, t) = q_{\text{bottom}} \tag{4}$$

$$-\alpha \frac{\partial h}{\partial r}(z, R, t) = q_{\text{wall}} \tag{5}$$

$$-\alpha \frac{\partial h}{\partial r}(z, 0, t) = 0 \tag{6}$$

$$-\alpha \frac{\partial h}{\partial z}(0, r, t) = q_{\text{top}} \tag{7}$$

where H is the height of the ingot, V_i is the speed at which the ingot grows, $\dot{m}_e$ is the casting rate, A_i is the cross sectional area of the ingot, h is the enthalpy per unit mass, and α is the thermal diffusivity.

The given boundary conditions define the heat fluxes on the different surfaces of the ingot. In the case of the top boundary condition, the total flux is the sum of the heat due to advection from molten metal inflow, direct plasma arc heat and radiative exchange with the surroundings. The heat transfer to the wall is the sum of contact heat transfer, helium cooling, and radiation exchange. Kinetic theory of rarefied gases is used to compute the heat transfer coefficient in the gap between the ingot and the crucible when helium is used as a coolant [13]. In the bottom of the ingot a uniform heat flux is applied. The last boundary condition applied is the symmetry with respect to the axis.

The heat equation in cylindrical coordinates, for a system that is symmetric with respect to its axis, when no convection is included, has the following form:

$$\frac{\partial h}{\partial t} = \frac{\partial}{\partial z}\left(\alpha\frac{\partial h}{\partial z}\right) + \frac{1}{r}\frac{\partial}{\partial r}\left(r\alpha\frac{\partial h}{\partial r}\right) \tag{8}$$

The solution to this transient heat conduction equation can be split into two regions: one for the solid and one for the liquid. Each region is governed by the same equation, and the differences lie in the diffusivity, α, and in the boundary conditions applied to each domain.

2.1 Thermal Conduction in the Solid and Liquid Regions. Assuming α_s for the constant thermal diffusivity of the solid phase and c for the constant-volume specific heat, the heat conduction equation in this region can be expressed in terms of enthalpy, which is evaluated with respect to a reference temperature T_0.

$$T = T_0 + \frac{1}{c}h, \quad \text{for } h < h_s \tag{9}$$

$$\frac{\partial h}{\partial t} = \alpha_s\left[\frac{\partial^2 h}{\partial z^2} + \frac{1}{r}\frac{\partial h}{\partial r} + \frac{\partial^2 h}{\partial r^2}\right] \tag{10}$$

A similar procedure is performed in the liquid region, where a constant thermal diffusivity α_l and the same c for the constant-volume specific heat are used to evaluate enthalpy as a function of temperature, taking the enthalpy at the liquidus temperature, h_l, as a reference

$$T = T_m + \frac{1}{c}(h - h_l), \quad \text{for } h > h_l \tag{11}$$

$$\frac{\partial h}{\partial t} = \alpha_l\left[\frac{\partial^2 h}{\partial z^2} + \frac{1}{r}\frac{\partial h}{\partial r} + \frac{\partial^2 h}{\partial r^2}\right] \tag{12}$$

The thermal model is described by a two-dimensional moving-boundary problem, because the location of the interface $S_{pool}(r,t)$ changes with time. As a result, the solid and liquid regions change their size. This problem can be simplified by transforming the moving-boundary problem to a fixed-boundary problem with the transformation described in Eqs. (13) and (14) [14]. The radial and time variables are nondimensionalized too.

$$x_s(z,r,t) = \frac{z - S_{pool}}{S} = \frac{z - S_{pool}}{H - S_{pool}} \tag{13}$$

$$x_l(z,r,t) = \frac{-z + S_{pool}}{S_{pool}} \tag{14}$$

$$\eta(r) = \frac{r}{r_i} \tag{15}$$

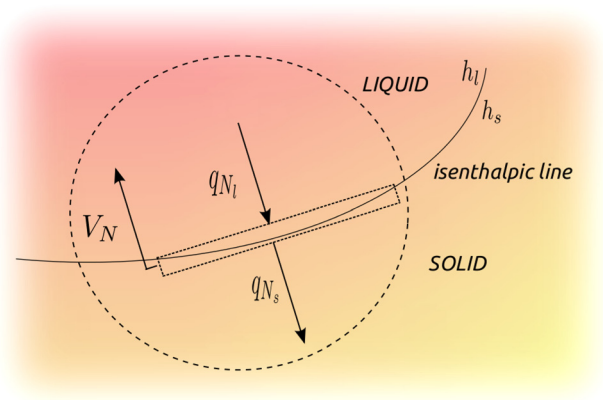$$\tau(t) = \frac{\alpha_s t}{r_i^2} \tag{16}$$

Fig. 3 Analysis of the interface

2.2 Heat Transfer in the Interface Region. The governing equation can be derived from a power balance at the liquid-solid interface. Along this interface the temperature, T_m, is constant and the enthalpy is constant on each side (h_l on the liquid side and h_s on the solid side); and as a consequence, there is no heat transfer along the interface and all heat transfer must be normal to it. This power balance, shown in Fig. 3, can be expressed by

$$V_N h_f = q_{N_s} - q_{N_l} \tag{17}$$

where N indicates velocity and heat flow normal to the interface and h_f is enthalpy of fusion per unit volume.

A model of displacement of the solidification front is shown in Fig. 4(a). Also, a blow up of a small region of this interface is shown in Fig. 4(b). The length of the element is such that the
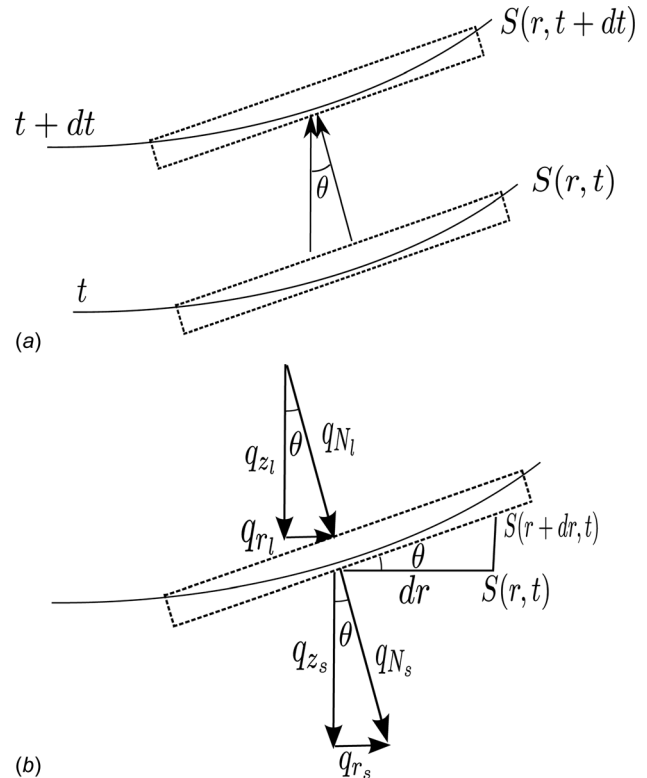

Fig. 4 Power balance at the interface

curvature of the interface can be neglected. Useful relations can be derived from the geometry of similar triangles

$$\lim_{dr \to 0} \frac{S(r+dr,t) - S(r,t)}{dr} = \frac{\partial S}{\partial r} = \frac{q_{r_s}}{q_{z_s}} = \frac{q_{r_l}}{q_{z_l}} \quad (18)$$

$$q_{N_s} = q_{z_s}\sqrt{1 + \left(\frac{\partial S}{\partial r}\right)^2} \quad (19)$$

$$q_{N_l} = q_{z_l}\sqrt{1 + \left(\frac{\partial S}{\partial r}\right)^2} \quad (20)$$

The velocity V_n at which the interface is moving can be obtained from the geometry of similar triangles as well

$$V_n = \frac{\partial S}{\partial t} \bigg/ \sqrt{1 + \left(\frac{\partial S}{\partial r}\right)^2} \quad (21)$$

Substituting Eqs. (19)–(21) and applying Fourier's Law to Eq. (17) returns a new expression dependent only on enthalpy and isenthalpic line $S(r,t)$. The superscripts $^+$ and $^-$ are used to indicate that the solid region and liquid region are used to evaluate the derivative, respectively.

$$\frac{\partial S}{\partial t} h_f = \left[1 + \left(\frac{\partial S}{\partial r}\right)^2\right]\left[-\alpha_s \frac{\partial h}{\partial z}\bigg|_{\left(S_{\text{pool}}^+, r, t\right)} + \alpha_l \frac{\partial h}{\partial z}\bigg|_{\left(S_{\text{pool}}^-, r, t\right)}\right] \quad (22)$$

3 Spectral Methods Solution

Spectral methods are numerical techniques used in applied mathematics to solve partial differential equations. Unlike finite element methods, spectral methods generate algebraic equations with full matrices, but in compensation, the high order of the basis functions gives higher accuracy. Use of global functions results in a geometric convergence rate instead of the algebraic one obtained with local basis functions. This property is particularly appealing when an accurate low-order approximation is required [15].

The partial differential equations are solved in a "weak form", for test functions Ψ_s and Ψ_l, using the Galerkin method. A weak form consists on multiplying a function, which is known to be equal to zero, by a test function, integrating the result over the physical domain and setting the integral as equal to zero. The weak form of the heat equation for the solid and liquid regions takes the form

$$\iint_{\Omega_{s,l}} \Psi_{s,l}\left(\frac{\partial h}{\partial t} - \nabla \cdot (\alpha_{s,l}\nabla h)\right)d\Omega_{s,l} = 0$$

$$\iint_{\Omega_{s,l}} \left\{\Psi_{s,l}\frac{\partial h}{\partial t} + \alpha_{s,l}\nabla\Psi_{s,l} \cdot \nabla h\right\}d\Omega_{s,l}$$

$$- \int_{\Gamma_{s,l}} \Psi_{s,l}\alpha_{s,l}\nabla h \cdot \hat{n}d\Gamma_{s,l} = 0 \quad (23)$$

The accuracy of the spectral method depends on the set of basis functions and the order selected for the approximation. Legendre polynomials, P_n^*, are suggested in Ref. [15] for symbolic calculations. However, due to the nonsymmetric nature of the boundary conditions of this problem, shifted Legendre polynomials in the domain $x_{s,l} \in [0,1]$ are more convenient for these heat transfer equations.

3.1 Enthalpy Distribution in the Solid Region.
The boundary conditions for the energy equation in the solid region are non-homogeneous. For convenience, the solution of this equation can

be split into two parts, a inhomogeneous term, h_s, and a homogeneous one, $h_f u$

$$h_{\text{solid}} = h_s + h_f u(x_s, \eta, \tau) \quad (24)$$

where the Dirichlet boundary condition is defined by

$$h_{\text{solid}}(0, \eta, \tau) = h_s \quad (25)$$

The homogeneous solution u is then approximated by the product series defined in terms of the basis functions $\phi_n(x_s)$ and $P_m^*(\eta)$

$$u = \sum_{n=0}^{N_s}\sum_{m=0}^{M_s} b_{nm}(\tau)\phi_n(x_s)P_m^*(\eta) \quad (26)$$

The order of the finite-dimensional expansion is given by $N_s = 2$ and $M_s = 1$, which correspond to the minimum order required to mimic the thermal dynamics of the solidifying ingot. The basis functions must satisfy the Dirichlet boundary condition, therefore $\phi_n(0) = 0$. In this case, ϕ_n is defined as

$$\phi_n = \begin{cases} P_n^* - P_0^*, & n = 0, 2, 4, \ldots \\ P_n^* + P_0^*, & n = 1, 3, 5, \ldots \end{cases}$$

while P_m^* denotes the standard shifted Legendre polynomials. The test function is defined as $\Psi_{s_{nm}} = \phi_n(x_s)P_m^*(\eta)$. The weak form of the heat equation now takes the form shown in below equation:

$$\int_0^R \int_{S_p(r,t)}^{H(t)} \left\{\Psi_s\frac{\partial h}{\partial t} + \alpha_s\left(\frac{\partial\Psi_s}{\partial z}\frac{\partial h}{\partial z} + \frac{\partial\Psi_s}{\partial r}\frac{\partial h}{\partial r}\right)\right\}2\pi r\,dz\,dr$$

$$+ \int_{S_p(r,t)}^{H(t)} \Psi_s q_{\text{wall}}\big|_{r=R}2\pi R\,dz = 0 \quad (27)$$

The dimensionless variables are substituted into the integro-differential equation, and the numerical expansions for the trial and basis functions are substituted too. The integrals in the equation can be solved symbolically, except for the last one which has to be done numerically due to the nonlinear boundary conditions, to obtain a system of ordinary differential equations for $db_{nm}/d\tau$. The resulting system of ordinary differential equations is equivalent to having a nonlinear dynamic system with state variables b_{nm}.

3.2 Enthalpy Distribution in the Liquid Region.
The boundary conditions for the energy equation in the liquid region are nonhomogeneous as well, and the solution can be split conveniently into two parts too

$$h_{\text{liquid}} = h_l + h_f v(x_l, \eta, \tau) \quad (28)$$

with a Dirichlet boundary condition

$$h_{\text{liquid}}(1, \eta, \tau) = h_l \quad (29)$$

A similar approximation is constructed for the homogeneous solution

$$v = \sum_{n=0}^{N_l}\sum_{m=0}^{M_l} a_{nm}(\tau)\psi_n(x_l)P_m^*(\eta) \quad (30)$$

The orders used for finite-dimensional expansion are $N_l = 2$ and $M_l = 2$. The boundary conditions used for this region must, once again, satisfy the Dirichlet boundary condition given in the form of $\psi_n(1) = 0$. As a result, ψ_n is defined as

$$\psi_n = P_n^* - P_0^*$$

The test function is defined as the product of the radial and axial basis function, similarly to what was done in the solid region. The weak form of the heat equation in the liquid region is shown in Eq. (31). Similarly to the previous case, dimensionless variables and finite-dimensional approximations are substituted into the equation to solve the integrals and derivatives. Symbolic manipulation can be performed for the first term, but the last two have to be computed numerically because of the nonlinear boundary conditions.

$$\int_0^R \int_0^{S_p(r,t)} \left\{ \Psi_l \frac{\partial h}{\partial t} + \alpha_l \left(\frac{\partial \Psi_l}{\partial z} \frac{\partial h}{\partial z} + \frac{\partial \Psi_l}{\partial r} \frac{\partial h}{\partial r} \right) \right\} 2\pi r \, dz \, dr$$
$$- \int_0^R \Psi_l q_{\text{top}}|_{z=0} 2\pi r \, dr + \int_0^{S_p(r,t)} \Psi_l q_{\text{wall}}|_{r=R} 2\pi R \, dz = 0 \quad (31)$$

Numerical manipulation results in a dynamic system with state variables a_{nm}.

3.3 Geometry of the Interface Region. The energy equation that describes the power balance in the interface region has only homogeneous boundary conditions and an approximate solution is sought in the form

$$S_{\text{pool}} = R \sum_{m=0}^{M} c_m(t) P_m^*(r) \quad (32)$$

The order used for the finite-dimensional expansion is $M = 2$. The weak form of the partial differential equation, evaluated with a test function γ, can then be expressed as

$$\int_0^R \gamma \left\{ h_f \frac{\partial S_p}{\partial t} - V_i h_f - \left[1 + \left(\frac{\partial S_p}{\partial r} \right)^2 \right] \left[\alpha_s \frac{\partial h}{\partial z} (S_p^+, r, t) \right. \right.$$
$$\left. \left. - \alpha_l \frac{\partial h}{\partial z} (S_p^-, r, t) \right] \right\} 2\pi r \, dr = 0$$

Evaluation of the integrals results in a system of ordinary differential equations for the time-dependent coefficients c_m, which define the geometry of the liquid pool profile.

3.4 Construction of a State Vector. The state vector of the nonlinear system, x, is defined by the spectral coefficients, which when multiplied by the basis functions expand the approximate solutions for enthalpy distributions and liquid pool profile, and the electrode thermal boundary layer, which links the system to the electrode melting process by providing information about the temperature distribution in the electrode as described by Beaman et al. [16] This new variable is introduced to model the complete VAR process by analyzing not only the ingot solidification but also the electrode melting.

$$\mathbf{x} = \begin{bmatrix} c, \text{ pool depth coefficients} \\ a, \text{ liquid coefficients} \\ b, \text{ solid coefficients} \\ \Delta, \text{ electrode thermal boundary layer} \end{bmatrix} \quad (33)$$

4 Linearization and Order Reduction

The dynamic equations obtained using spectral methods are nonlinear and have the classic state space form

$$\dot{x} = f(x, u) \quad (34)$$
$$y = h(x, u) \quad (35)$$

where x is the state vector, and u is the input vector consisting of the current and the melt efficiency. The melt efficiency, defined as the ratio between the melt power (P_{melt}) and the total power, is a variable used to link the melting process (in the electrode) to the solidification process (in the ingot) by defining the amount of power that goes in melting the electrode. The reason why it is considered an input in this linearized system is because it is not dependent on the state variables. This value, however, cannot be modified externally, so μ is an uncontrolled disturbance input.

$$\mu = \frac{P_{\text{melt}}}{VI} \quad (36)$$

The output y shown in Eq. (35) is the array containing pool depth measurements at different radii. These are the values that will be monitored to control the solidification process.

The dynamic equations are simplified when the set of nonlinear differential equations are linearized about nominal conditions.

$$\delta\dot{x} = A\delta x + B\delta u \quad (37)$$
$$\delta y = C\delta x \quad (38)$$

Once the system is linearized, their perturbations from nominal conditions are the ones that will appear in the system of linear equations. The nominal operating point is defined by the user based on typical values of melting current and melt rate. These perturbations are defined as

$$\delta x = x - x_0 \quad (39)$$
$$\delta u = u - u_0 = \begin{bmatrix} \delta I \\ \delta \mu \end{bmatrix} \quad (40)$$
$$\delta y = y - y_{\text{ref}} \quad (41)$$

Solidification processes usually have eigenvalues with a very slow response because they are associated with diffusion processes, which are very slow. These slow modes will be the ones that will dominate the response of the system. The linear model is transformed into its diagonal form, where the transformed state vector contains modal state variables which can be partitioned into a set of reduced states x_1, the dominant modes to be considered in the reduced-order model; and remaining states x_2, which are fast modes to be suppressed. If the dynamics of the states x_2 are much faster than those of the reduced states x_1, then x_2 will have settled in steady state much sooner than the reduced-order states x_1. As long as this relationship holds, the reduced-order model shown in Eq. (42) will have the same dynamic characteristics as the original full-order model in the primary control bandwidth.

$$\delta\dot{x}_1 = A_r \delta x_1 + B_r \delta u \quad (42)$$
$$\delta y = C_r \delta x_1 \quad (43)$$

The corner time constant (τ_{fast}) used to reduce the order of the dynamic system was set equal to 40 s, so any mode with a time constant faster than 40 s was suppressed. Once modal reduction had been applied the order of the system was reduced from 14 to 6. From here on the subindex 1 will be dropped from the state space equations of the reduced-order model but it should be clear that the fast modes have already been removed from the system.

5 Comparison With BAR

The reduced-order model, whose dynamic equations are much simpler than the ones of BAR, is simple enough to be used in real-time estimation and control. However, before the model is implemented we need to be sure that the response of the reduced-order model resembles that of the high-fidelity model. In order to verify
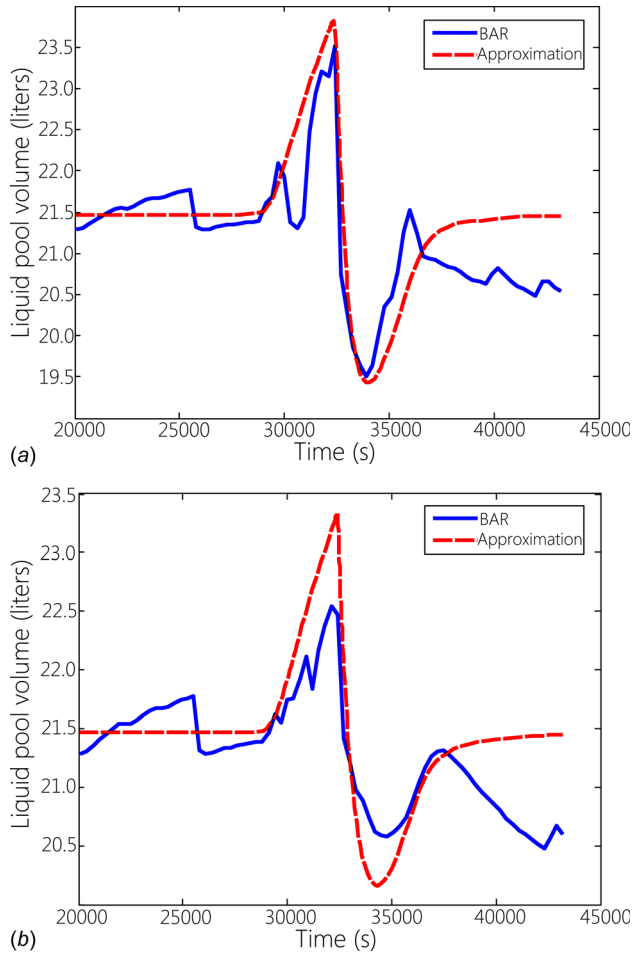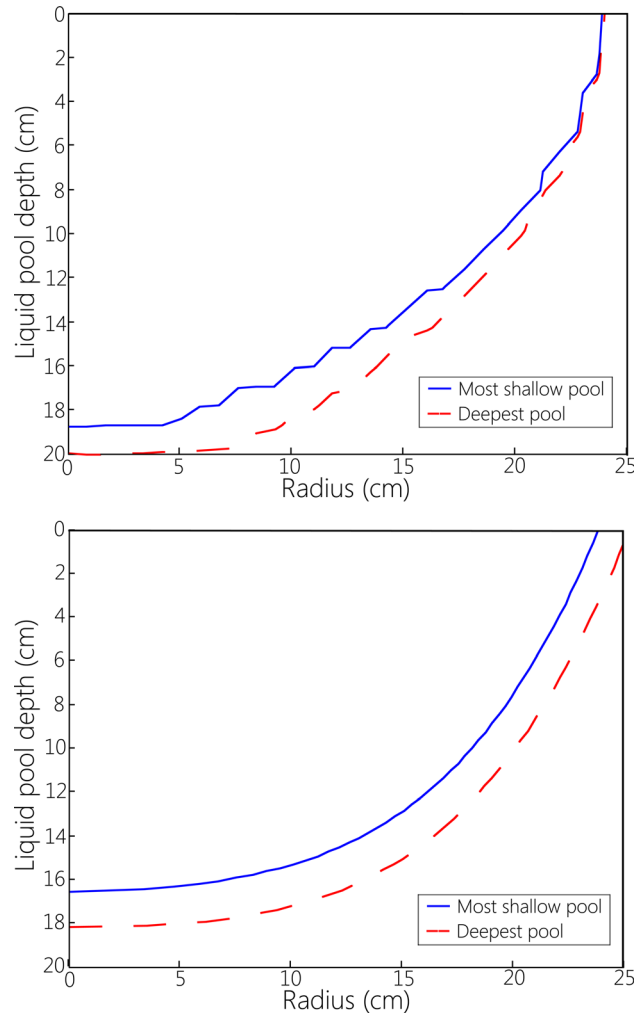
Fig. 5 Comparison between the high-fidelity model (BAR) and the reduced-order one for $\tau_{\text{fast}} = 40$s

Fig. 6 Comparison of predicted pool profiles

that the reduced-order model effectively resembles the response of BAR, simulations have been run considering both deviations in current and melt rate from nominal conditions and how they would affect the total liquid pool volume. Results are shown in Fig. 5. For this comparisons, both systems were run using nominal operating conditions until quasi-steady state was reached, and then only one of the inputs was increased by 10% with a ramp in a 20 min interval, to then be decreased to 90% of the original value in a second 20 min interval, and finally be taken back to nominal conditions in a third 20 min long ramp, while the other input was kept constant. In the first case it was the value of the current that was changed, while in the second one it was the melt rate (proportional to melt efficiency).

It can be seen that the reduced-order model shows a response that is similar to one of the high-fidelity model, except for the high-frequency modes. The geometry of the predicted pool shape for both models was compared as well and the result is shown in Fig. 6. Both the deepest and the most shallow pool profiles predicted for the simulation shown in Fig. 5 are plotted, showing that not only the total volume of liquid predicted with both models is similar but also the shape of the predicted liquid pools. The pool shapes are similar but the one predicted with the reduced-order model is slightly shallower.

6 Pool Profile Control

Ingot solidification is the crucial part of the process that defines the microstructural properties of the material. Nonetheless, ingot solidification is not directly controlled in industrial practice of VAR. It was common for remelting companies to control the DC

current sent to the furnace and assume that, by doing so, the solidification front will be controlled. Modern day VAR practice usually calls for some form of melt rate control using load cell feedback. Current control is still employed at the beginning and end of melting where melt rate control using load cell feedback is difficult. Extensive testing was used for companies to develop what is called a melt recipe, which defined how melt rate and current should be changed during the melt in order to obtain a defect-free microstructure. Such an approach lacks robustness and treats the whole process as a black box.

In the past years, a new generation of model-based controllers was developed to control solidification in vacuum arc remelting by controlling melt rate or the total amount of power flowing into the liquid pool. These controllers were seen as significant improvements in the industry of remelting processes but there was still no way to control solidification. The main impediment came from the lack of an appropriate ingot solidification model that could be used for estimation and control of VAR.

The reduced-order thermal model proposed in this paper can be used to design a model-based controller for the liquid pool profile in vacuum arc remelting. In this case, electrode gap is controlled by changing the ram speed in the furnace [17]. However, control of ingot solidification involves using the new reduced-order model to invert the dynamic equations of the system and compute the required value of current that would drive the system to desired conditions. The model used for control is only an approximation of the highly complex dynamics of VAR and all measurements in this process are known to be noisy. Therefore, uncertainty will

play an important role in the design of the process controller for this multivariable plant. A linear-quadratic-gaussian strategy is proposed to design an optimal controller solving the linear quadratic regulator equations, and a Kalman Filter for optimal state estimation. The LQG controller, described in the block diagram given in Fig. 7, will return the required optimal input even under model uncertainty and noisy measurements (Fig. 7).

Current corrections are computed to make liquid pool depth coincide with the desired values at m radii r_i as shown

$$I = I_0 + \delta I$$

$$\delta I = -K_x \delta x - K_\mu \delta \mu - K_{\text{ref}} \delta y_{\text{ref}}$$

$$\delta y_{\text{ref}} = \begin{bmatrix} \delta S_{\text{pool}_{\text{ref}}}(r_1, t) \\ \cdots \\ \delta S_{\text{pool}_{\text{ref}}}(r_m, t) \end{bmatrix}$$

where the control gains matrices K_x, K_μ, and K_{ref} are chosen to minimize the cost function shown in Eq. (44) in a linear quadratic regulator problem. As a first approach, only one radial location will be controlled ($m = 1$). The weighting matrices $\mathbf{Q}$ and $\mathbf{R}$ are defined as diagonal positive-definite matrices and their values were adjusted based on the desired time in which state perturbations are reduced to small values and the desired speed for the controller [18].

$$J = \int_0^\infty \delta y^T \mathbf{Q} \delta y + \delta I^T \mathbf{R} \delta I dt \qquad (44)$$

7 Pool Profile Estimation

So far, the controller has been designed under the assumption that both the model and measurements are perfect, i.e., process and measurement noises are zero. Given precise measurements of all the state variables, the control law defined in Sec. 6 could give an excellent steady-state control. However, electrode gap measurements, based on voltage or drip-short frequency, are inherently noisy and uncertain, and there is no way to measure the liquid pool depth directly.

A Kalman filter is used to estimate, on the basis of noisy measurements, the values of the state variables of a system subject to stochastic input disturbances. The computation of the Kalman gains in a time-invariant system, such as this one, converges to steady-state if the system is completely observable. It is often satisfactory to use a simplified time-invariant filter, based on the assumption of time-invariant statistics of the noise terms, to obtain a constant gain matrix.
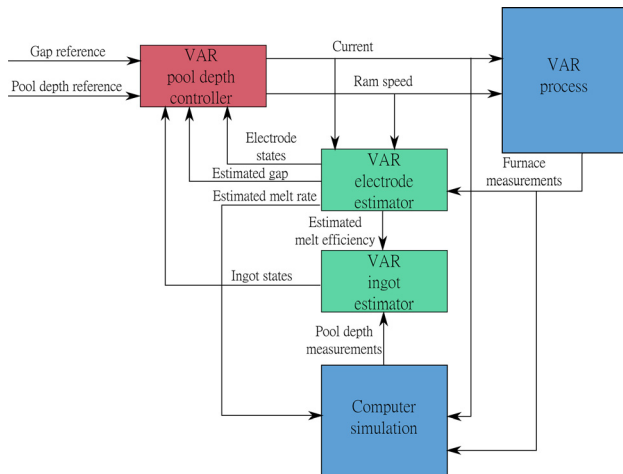

Fig. 7 Pool depth control of VAR

In the Kalman filter, everything is developed under the assumption that all random variables are modeled as white noise processes. However, the change in melt efficiency is better described by a random walk process, so a way to express perturbation in melt efficiency as a white noise is required. The increments in a random walk are Gaussian random variables. Heuristically, one can generate a random walk by passing white noise through an integrator [19]. Hence, although we cannot model melt efficiency as a white noise sequence we can still do so with its increments. Since the derivative of μ will have to appear in the continuous-time equation shown in Eq. (42) it would be convenient to augment the state vector with an extra variable: perturbation in melt efficiency.

In this case, it is assumed that process uncertainty comes only from inaccuracies in the values of I and μ, therefore the process noise vector $\mathbf{w}$ will only have two components.

For simplicity, the dynamic system is transformed into a discrete-time process, for a time step of $\Delta t = 2s$, because most measurements are available only at discrete times and the thermal behavior of the system changes slowly. The continuous-time equations are transformed into the discrete-time dynamic equations of the augmented system

$$\begin{bmatrix} \delta x \\ \delta \mu \end{bmatrix}_{n+1} = \begin{bmatrix} \delta x \\ \delta \mu \end{bmatrix}_n + \begin{bmatrix} A & B_\mu \\ 0 & 0 \end{bmatrix} \Delta t \begin{bmatrix} \delta x \\ \delta \mu \end{bmatrix}_n$$

$$+ \begin{bmatrix} B_I \\ 0 \end{bmatrix} \Delta t \delta I_n + \begin{bmatrix} B_I & 0 \\ 0 & 1 \end{bmatrix} \begin{bmatrix} w_I \Delta t \\ w_\mu \end{bmatrix}_n$$

$$\Phi = I + \begin{bmatrix} A & B_\mu \\ 0 & 0 \end{bmatrix} \Delta t$$

$$\Lambda = \begin{bmatrix} B_I \\ 0 \end{bmatrix} \Delta t \qquad (45)$$

$$\Gamma = \begin{bmatrix} B_I & 0 \\ 0 & 1 \end{bmatrix}$$

$$\begin{bmatrix} \delta x \\ \delta \mu \end{bmatrix}_{n+1} = \Phi \begin{bmatrix} \delta x \\ \delta \mu \end{bmatrix}_n + \Lambda \delta I_n + \Gamma \begin{bmatrix} w_I \Delta t \\ w_\mu \end{bmatrix}_n$$

$$\mathbf{x}_{n+1} = \Phi \mathbf{x}_n + \Lambda \mathbf{u}_n + \Gamma \mathbf{w}_n$$

The measurement equation is modified as well to include melt efficiency, which is now a state that can be "measured" from the electrode estimator designed in Ref. [17]. Uncertainty caused by noisy measurements, both for pool depth and melt efficiency, is included in the form of the vector $\mathbf{v}$.

$$\begin{bmatrix} \delta y \\ \delta \mu \end{bmatrix}_n = \begin{bmatrix} C & 0 \\ 0 & 1 \end{bmatrix} \begin{bmatrix} \delta x \\ \delta \mu \end{bmatrix}_n + \begin{bmatrix} v_{PD} \\ v_\mu \end{bmatrix}_n \qquad (46)$$

$$\mathbf{z}_n = \mathbf{H} \mathbf{x}_n + \mathbf{v}_n$$

One more set of matrices are required to derive the Kalman gain matrix, namely, the covariance matrices corresponding to the process and measurement noise vectors $\mathbf{w}_n$ and $\mathbf{v}_n$. Noise terms are modeled as zero-mean white-noise random sequences. As a result they are defined completely by their covariance matrices. The process covariance, usually denoted $\mathbf{Q}$, is given by

$$\mathbf{Q} = \begin{bmatrix} (\sigma_I \Delta t)^2 & 0 \\ 0 & \sigma_\mu^2 \end{bmatrix} \qquad (47)$$

where σ denotes the standard deviation of every noise term: one for current and another one for melt efficiency. In the case of the measurement covariance, usually denoted $\mathbf{R}$

$$\mathbf{R} = \begin{bmatrix} \sigma_{PD_1}^2 & \cdots & 0 & 0 \\ \vdots & \ddots & \vdots & \vdots \\ 0 & \cdots & \sigma_{PD_m}^2 & 0 \\ 0 & \cdots & 0 & \sigma_\mu^2 \end{bmatrix} \qquad (48)$$

contains the uncertainties related to the pool depth measurements at m radii and the estimated melt efficiency, that is estimated by an electrode estimator as described in Ref. [16].

Note the matrices are diagonal, that is, we are specifying that there are no interaction terms. Also, it is implicitly specified that the process and measurement noise terms are independent of each other. Therefore, there is no cross-covariance matrix. The noise covariance, including both process and measurement noise terms, takes the following form:

$$\mathrm{E}\left\{ \begin{bmatrix} \Lambda\mathbf{w}_n \\ \mathbf{v}_n \end{bmatrix} \begin{bmatrix} \mathbf{w}_n^T\Lambda^T & \mathbf{v}_n^T \end{bmatrix} \right\} = \begin{bmatrix} \Lambda\mathbf{Q}\Lambda^T & 0 \\ 0 & \mathbf{R} \end{bmatrix}$$

The state residuals are defined as

$$\varepsilon^{(-)} = \mathbf{x}_n - \hat{\mathbf{x}}_n^{(-)}$$

$$\varepsilon^{(+)} = \mathbf{x}_n - \hat{\mathbf{x}}_n^{(+)}$$

where

$$\hat{\mathbf{x}}_n^{(-)} = \Phi\hat{\mathbf{x}}_{n-1}^{(+)} + \Lambda\mathbf{u}_{n-1}$$

$$\hat{\mathbf{x}}_n^{(+)} = \hat{\mathbf{x}}_n^{(-)} + \mathbf{K}\left[\mathbf{z}_n - \mathbf{H}\hat{\mathbf{x}}_n^{(-)}\right]$$

$\hat{\mathbf{x}}_n^{(-)}$ is the state estimate prior to the measurement update (prediction), and $\hat{\mathbf{x}}_n^{(+)}$ is the state estimate after the measurement update. The steady-state gains, $\mathbf{K}$, are used in this semi-optimal approach.

The levels of process noise and measurement noise used for the design of the Kalman filter are shown in Tables 1 and 2. The noise strengths are the standard deviation of the parameters. Some of these standard deviations were obtained from experiments, as in the case of the current. Melt efficiency noise strength was obtained from computer simulation, and the others were defined based on empirically realistic values.

8 Liquid Pool Depth Virtual Measurements

An obvious inconvenience with the proposed controller and estimator is that no direct measurements are available for the liquid pool profile of the ingot in the furnace. If no measurements are available from the furnace then the system is unobservable and, therefore, accurate process control is not possible. Although today's technology does not provide with an accurate way of measuring the pool profile or the temperature distribution in the ingot, a high-fidelity computational model such as BAR could be used to improve the observability of the system and the overall performance of the controller. BAR, which is the closest approximation available to the actual melt, would be used as a noninvasive method to provide virtual measurements of the parameters that cannot be measured in any other way. Because liquid pool profile is known to be related to defect formation in VAR, it will be monitored and controlled throughout the melt. If other parameters are reported to be related to other solidification defects, they would be included in the high-fidelity model and the control system in a similar way.

BAR was not intended to be used in process control systems but to study the physical conditions that would lead to the formation of defects in remelting processes [6]. The structure of the model had to be modified so that it could be run in parallel to the actual melt. BAR is run with the same inputs that are sent to the actual furnace (i.e., current, voltage, melt rate, and helium pressure) to ensure that the model and the furnace are synchronized. BAR is used to provide a measurement of the temperature distribution in the solidifying ingot. These temperature measurements can be used to get an estimate of the liquid pool profile using a linear interpolation to find the location where the liquidus temperature occurs. The pool depth measurements can be obtained for as many radial locations as required.

In the case presented in this paper, only two virtual measurements were used to improve the observability of the control system. The locations where the measurements are taken are carefully chosen to get measurements that are representative to describe the liquid pool profile. The centerline pool depth and that of $r = 0.7\, r_i$ are used. The centerline pool depth provides information about the maximum liquid pool depth in the ingot, and $0.7\, r_i$ is a representative mean radius for which the internal cross-sectional area is the same as the external cross-sectional area. The two virtual measurements are not treated with the same uncertainty, as shown in Table 2. The physical properties used for the thermal model were calibrated to match BAR liquid pool depth predictions at $0.7\, r_i$ in steady-state, but the same properties result in an offset for the pool depth predictions at the centerline. In order to follow closely the prediction at the mean radius, a very small uncertainty is used for this virtual measurement compared to the one of the centerline.

BAR is based on finite volume methods, which discretize the ingot. As a consequence, there is a small oscillation in the pool depth measurement every time the estimated pool profile jumps from one grid element to another one. Although the oscillation is small, it is undesired since if it is not attenuated it can cause the controller to oscillate as well. In order to obtain a more stable response a prefilter is used for the pool depth measurements. The prefilter attenuates any fast dynamics with an infinite impulse response digital Butterworth low pass filter [20].

9 Implementation of the Pool Depth Controller

The LQG pool depth controller was successfully implemented in a laboratory-scale furnace in Los Alamos National Laboratory using Alloy 718 in July 2011. Information about the furnace and the material used for the test are given in Tables 3 and 4.

Only one pool depth was monitored and controlled in the implementation of the proposed controller. The pool depth at $0.7\, r_i$ was chosen as the most representative pool depth because it is an average value. Although only one pool depth will be monitored in the controller, two measurements will be used in the estimator.

The experiment was started with constant current control mode. The exact moment when pool depth control mode started is marked with the *pool depth control mode turned ON* note in

Table 1 Process noise levels

Parameter	Noise strength
Current (w_I)	120 A
Melt efficiency rate (w_μ)	0.01 μ_0

Table 2 Measurement noise levels

Parameter	Noise strength
Pool depth at 0.0 r_i (n_{PD})	6.0 cm
Pool depth at 0.7 r_i (n_{PD})	0.2 cm
Estimated melt efficiency (n_μ)	2.33×10^{-5}

Table 3 Furnace parameters

Parameter	Value
Electrode radius	7.62 cm
Ingot radius	10.8 cm
Nominal current	2800 A
Nominal voltage	23.5 V
Nominal melt rate	34 g/s
Nominal electrode gap	1.0 cm

Table 4 Thermophysical properties of Alloy 718

| Property	Value
Melt temperature	1623 K
Density	7.75 g/cm^3
Heat capacity	0.65 J/g K
Latent heat	210 J/g
Solidus enthalpy	762.4 J/g
Liquidus enthalpy	1070.0 J/g
Thermal diffusivity (solid phase)	0.0637 cm^2/s
Thermal diffusivity (liquid phase)	0.0676 cm^2/s

Fig. 8. Virtual pool depth measurements are recorded from the beginning of the melt. However, they are included for estimation only when the measurements are close to the estimated pool shape, as marked by the *BAR feedback turned ON* note in Fig. 8. The reason for this is that the reduced-order model is based on a steady-state approximation so it is valid only close to steady-state. In the beginning of the melt the ingot is very small and just starting to solidify, so controlling the pool profile would not make much sense.

Experimental results, see Fig. 8, show that once the virtual measurements have been included in the estimator, the measured pool depth for the mean radius and the estimated one match. Even though these values coincide there is a difference in the centerline pool depth. This is an indicator that there is a mismatch between the dynamics predicted with the reduced-order model and that of BAR at the centerline. The differences between these two models can cause significant problems if pool profile is controlled at a wide range of radial locations.

The pool profile controller was tested for several liquid pool depths under step changes in the reference, showing a good transient response. A small amount of steady state error can be seen, but its value is negligible compared to the desired liquid pool depths. Small oscillations are shown after step changes in pool depth reference but they disappear quickly.
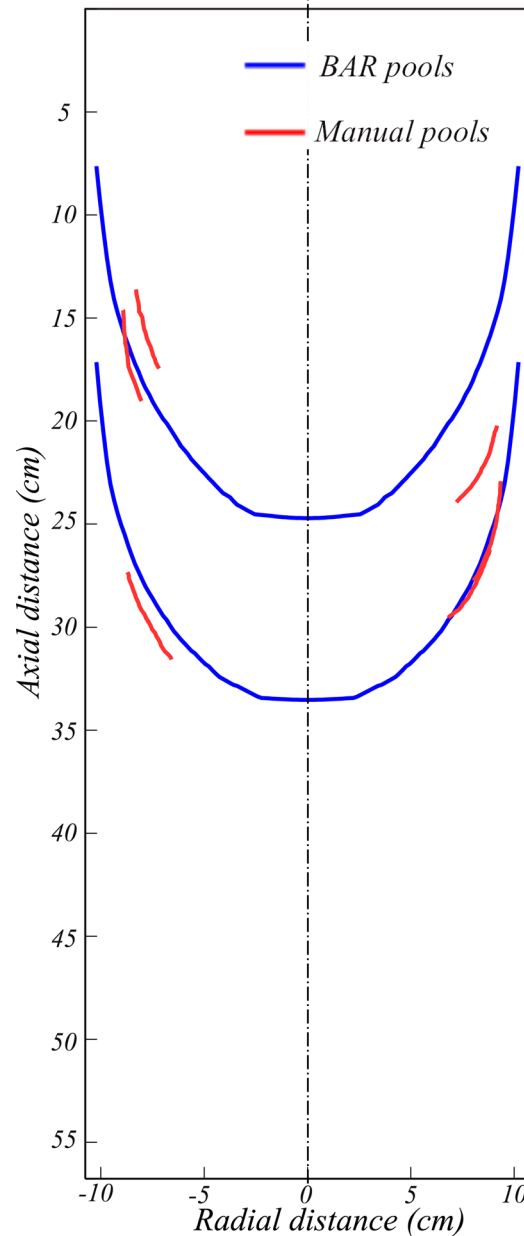
Fig. 9 Comparisons between liquid pool depths predicted with BAR and those measured experimentally
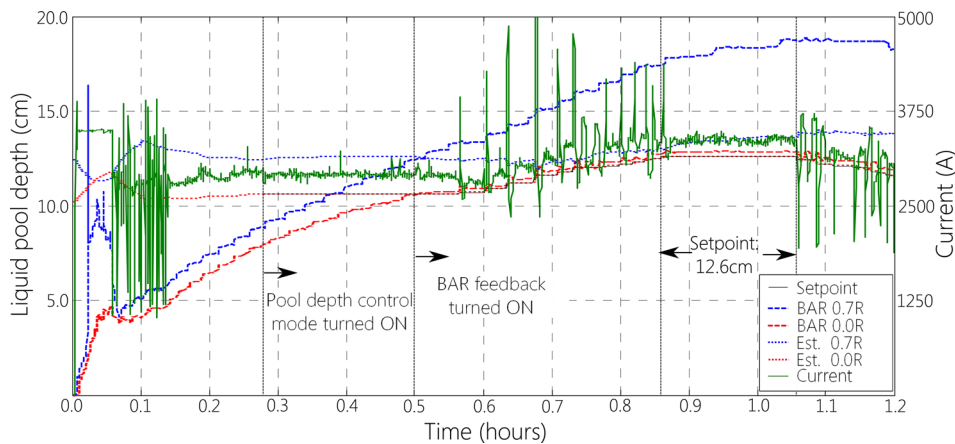
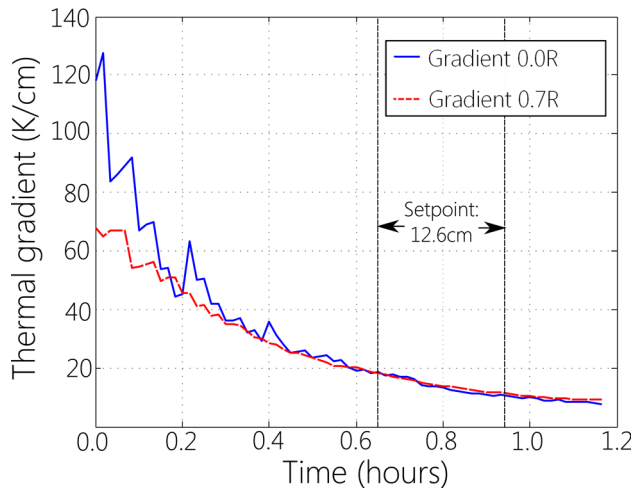Fig. 8 Experimental results

Fig. 10 Thermal gradient in experiment

In a real melt the desired liquid pool shape will, most likely, be kept a constant value in order to prevent macrosegregation. The case of a constant reference pool depth of 12.6 cm, a case of potential interest to industry applications, was tested. In this part of the experiment the controller showed a good performance and was able to maintain the predicted liquid pool depth close to the desired value. The current required to stabilize the system at the desired pool depth was approximately 3300 A.

A detailed analysis of the ingot including pool shape, solidification rate, and approximate thermal gradient is reported in Ref. [21]. However, the most important study is whether the pool profiles measured experimentally compare favorably to those predicted by the computational model. Liquid pool profiles were manually measured by tracking dark bands along the expected pool profile, attributed to channels or similar dark-etching regions. This technique is a common practice in the production of superalloys. It can be seen that in the central part of the ingot, in which melting conditions were close to steady state, pool depths observed experimentally compare well to those predicted with BAR, as shown in Fig. 9. Therefore, when close to steady state (which occurs for most of the melt) accurate control of the liquid pool profile predicted by BAR is expected to result in accurate control of the geometry of the solidification front.

The thermal gradient G, shown in Fig. 10, is a very important variable in the solidification of the metal ingot [22] and can be monitored in real-time with BAR. The thermal gradient in the mushy zone affects the dendrite arm spacing, which affects the tendency to create freckles. It can be seen that the value of the thermal gradient was just starting to converge to steady-state at the end of the experiment. The process controller was designed based on a model linearized about steady-state conditions, which were never met in the experiment. Such a behavior is expected for very small furnaces, were melts last for a few hours, but it would not happen in a full-size furnace, where the melts last longer and the ingot solidification often reaches quasi-steady conditions. The controller presented in this paper would make a better job if used in an industrial-sized furnace where most of the melt occurs in quasi-steady conditions. A transient controller would be required for cases in which quasi-steady conditions are never reached, i.e., small furnaces and when melting Titanium alloys.

10 Conclusions

A new generation of process controllers for vacuum arc remelting is proposed in this paper. For the first time, the liquid pool profile was controlled in order to prevent macrosegregation defects. This is a significant improvement from previous controllers which focus on the melting of the electrode and treat the ingot as a black box. An accurate real-time description of the solidification dynamics is obtained from BAR, a high-fidelity model run in parallel to the furnace. The model was incorporated in a CPU to provide virtual measurements of liquid pool profile in real time. These measurements, just like the ones coming from sensors, are subject to bias and noise. All measurements are combined optimally by using a Kalman filter.

The proposed controller was successfully implemented in a laboratory-scale furnace in Los Alamos National Laboratory in July 2011. Some general comments that can be drawn from the experimental results are that the reduced-order model, suitable and convenient for control and estimation, is not very precise on describing the solidification of the whole ingot. It can be seen that the estimated pool depth at 0.7 r_i matches the one predicted by BAR, but the centerline pool depth does not agree with BAR. The authors think that the difference between the pool depths predicted by the two models is caused by the attempt to model an anisotropic phenomenon, such as fluid flow in the liquid region, with an isotropic model that includes diffusion only.

It should also be noted that both the high-fidelity and the reduced-order models are two-dimensional but they are being used to prevent defects that are three-dimensional in nature. A three-dimensional model could be required for a better description of solidification defects and their sources.

Nomenclature

c = specific heat
$E[\cdot]$ = expectation
G = thermal gradient
h = enthalpy per unit mass
H = ingot height
h_f = enthalpy of fusion per unit volume
I = melting current
$\dot{m}_e$ = electrode melt rate
PD = pool depth
q_{bottom} = heat flux at the bottom of the ingot
q_{top} = total heat flux atop the ingot
q_{wall} = total sidewall heat flux
r_e = electrode radius
r_i = ingot radius
S_{pool} = liquid pool depth measured from the ingot top
T_m = melting temperature
V_i = velocity at which the ingot grows
α = thermal diffusivity
δ = perturbation from nominal conditions
Δ = electrode thermal boundary layer
μ = melt efficiency
$\hat{\cdot}$ = estimate

References

[1] Choudhury, A., 1990, *Vacuum Metallurgy*, ASM International, Materials Park, OH.
[2] Winkler, O., and Bakish, R., eds., 1971, *Vacuum Metallurgy*, Elsevier Publishing Company, New York.
[3] Yu, K.-O., Domingue, J. A., and Maurer, G., 1986, "Macrosegregation in ESR and VAR Processes," JOM, **38**(1), pp. 46–50.
[4] Kou, S., 1978, "Macrosegregation in Electroslag Remelted Ingots," Ph.D. thesis, Department of Materials Science and Engineering, MIT, Cambridge, MA.
[5] Yuan, L., Djambazov, G., Lee, P. D., and Pericleous, K., 2009, "Multiscale Modeling of the Vacuum Arc Remelting Process for Prediction on Microstructure Formation," Int. J. Mod. Phys. B, **23**, pp. 1584–1590.

[6] Bertram, L., Schunk, P., Kempka, S., Spadafora, F., and Minisandram, R., 1998, "The Macroscale Simulation of Remelting Processes," JOM, **50**(3), pp. 18–21.

[7] Kelkar, K. M., Patankar, S. V., Mitchell, A., Kanou, O., Fukada, N., and Suzuki, K., 2007, "Computational Modeling of the Vacuum Arc Remelting (VAR) Process Used for the Production of Ingots of Titanium Alloys," 11th World Conference on Titanium (Ti-2007), Kyoto, Japan, June 3–7.

[8] Adasczik, C., Bertram, L., Evans, D., Minisandram, R., Sackinger, P., Wegman, D., and Williamson, R. L., 1997, "Quantitative Simulation of a Superalloy VAR Ingot at the Macroscale," Proceedings of the AVS Vacuum Metallurgy Conference, Santa Fe, NM, February 16–19.

[9] Yu, K.-O., ed., 2002, *Modeling for Casting and Solidification Processing*, CRC Press, New York.

[10] Kondrashov, E. N., Musatov, M. I., Maksimov, A. Y., Goncharov, A. E., and Konovalov, L. V., 2007, "Calculation of the Molten Pool Depth in Vacuum Arc Remelting of Alloy Vt3-1," J. Eng. Thermophys., **16**(1), pp. 19–25.

[11] Minisandram, R. S., Arnold, M., and Williamson, R. L., 2005, "VAR Pool Depth Measurement and Simulation for a Large Diameter Ti-6Al-4V Ingot," Proceedings of the 2005 International Symposium on Liquid Metal Processing and Casting (LMPC 2005), Santa Fe, NM, September 18-21, ASM International, Materials Park, OH, Santa Fe, NM, February 21–24, pp. 1–6.

[12] Bertram, L., 1999, "Transient Melt Rate Effects on Solidification During VAR of 20 Inch Alloy 718," Proceedings of the 1999 International Symposium on Liquid Metal Processing and Casting, Santa Fe, NM, February 21–24, pp. 156–167.

[13] Yu, K.-O., 1986, "Comparison of ESR-VAR Processes. Part I: Heat Transfer Characteristics of Crucibles," Proceedings AVS Vacuum Metallurgy Conference on Speciality Metals Melting and Processing, Pittsburgh, PA, June 9–11, pp. 83–92.

[14] Duda, J. L., Malone, M. F., Notter, R. H., and Vrentas, J. S., 1975, "Analysis of Two Dimensional Diffusion Controlled Moving Boundary Problems," Int. J. Heat Mass Transfer, **18**, pp. 901–910.

[15] Boyd, J. P., 2001, *Chebyshev and Fourier Spectral Methods*, Dove, New York.

[16] Beaman, J. J., Williamson, R. L., Melgaard, D. K., and Hamel, J., 2005, "A Nonlinear Reduced Order Model for Estimation and Control of Vacuum Arc Remelting of Metal Alloys," 2005 ASME International Mechanical Engineering Congress and Exposition, Orlando, FL, November 5–11, ASME Paper No. IMECE2005-79239, pp. 1059–1067.

[17] Hysinger, C. L., Beaman, J. J., Williamson, R. L., and Melgaard, D. K., 1999, "Multiple Input Electrode Gap Control During Vacuum Arc Remelting," International Symposium on Liquid Metal Processing and Casting (LMPC 1999). Santa Fe, NM, February 21–24.

[18] Athans, M., 1971, "The Role and Use of the Stochastic Linear-Quadratic-Gaussian Problem in Control System Design," IEEE Trans. Autom. Control, **AC-16**, pp. 529–552.

[19] Maybeck, P. S., 1979, *Stochastic Models, Estimation and Control*, Vol. 1, Academic Press Inc., New York.

[20] Ingle, V. K., and Proakis, J. G., 2007, *Digital Signal Processing Using MATLAB*, Cengage Learning, New York.

[21] Watt, T. J., Taleff, E. M., Beaman, J. J., Lopez, L. F., Moser, R., Bauman, P., and Williamson, R. L., 2013, "Solidification Mapping of a Nickel 718 Laboratory VAR Ingot," Proceedings of the International Symposium on Liquid Metal Processing and Casting (LMPC 2013), Austin, TX, September 22–25.

[22] Van Den Avyle, J. A., Brooks, J. A., and Powell, A. C., 1998, "Reducing Defects in Remelting Processes for High-Performance Alloys," J. Mater., **50**(3), pp. 22–26.